Rare Metal Materials and Engineering
Volume 55, Issue 1, January 2026
Available online at www.rmme.ac.cn

Science Press

Cite this article as: Tu Yanni, Luo Wei, Liu Huiqun, et al. Low-Density Pulsed Current Induced Refinement of Secondary *α* Phase for Strengthening Ti-6Al-4V-0.5Mo-0.5Zr Alloy Without Sacrificing Ductility[J]. Rare Metal Materials and Engineering, 2026, 55(01): 78-91. DOI: https://doi.org/10.12442/j.issn.1002-185X.20250032.

ARTICLE

Low-Density Pulsed Current Induced Refinement of Secondary *α* Phase for Strengthening Ti-6Al-4V-0.5Mo-0.5Zr Alloy Without Sacrificing Ductility

Tu Yanni[1], Luo Wei[1], Liu Huiqun[1,2], Feng Weizhong[3], Zhang Pinghui[3]

[1] School of Materials Science and Engineering, Central South University, Changsha 410083, China; [2] State Key Laboratory of Powder Metallurgy, Central South University, Changsha 410083, China; [3] Baoji Titanium Industry Co., Ltd, Baoji 721014, China

Abstract: Low-density short-duration pulsed current-assisted aging treatment was applied to the Ti-6Al-4V-0.5Mo-0.5Zr alloy subjected to different solution treatments. The results show that numerous α_p phases redissolve into the new β phase during the pulsed current-assisted aging process, and then the newly formed β phase is mainly transformed into the β_t phase, with occasional transition to new α_p phase, leading to a remarkable grain refinement, especially for the lamellar α_s phases. In comparison to conventional aging treatment, the pulsed current-assisted aging approach achieves a significant enhancement in strength without degrading ductility, yielding an excellent mechanical property combination: a yield strength of 932 MPa, a tensile strength of 1042 MPa, and an elongation of 12.2%. It is primarily ascribed to the increased fraction of β_t phases, the obvious grain refinement effect, and the slip block effect induced by the multiple-variant α_s colonies distributed within β_t phases.

Key words: titanium alloy; pulsed current; microstructure refinement; strength; ductility

1 Introduction

Ti-6Al-4V alloys, which consist of $\alpha+\beta$ phases and exhibit excellent specific strength and corrosion resistance, have been widely used in aviation, aerospace, and petrochemical industries[1–2]. Alloying with trace elements allows the regulation of microstructures and the improvement of overall properties[3–6]. In particular, Ti-6Al-4V alloys doped with elements Mo and Zr have superior strength, making them promising candidate materials for oil drill pipes, such as Ti-6Al-4V-0.5Mo-0.5Zr[7–9]. Notably, the mechanical properties of these alloys are highly sensitive to their microstructures, such as the proportions, grain (or colony) sizes, and distribution characteristics of the primary α (α_p), secondary α (α_s), and transformed β (β_t) structures, which can be adjusted by solution and aging treatments. Jing et al[10] investigated the effect of the α phase on mechanical properties, revealing that the α_p phase has a greater deformability than the α_s phase: the α_p phase readily undergoes significant deformation (through slip and twin deformation) to achieve better ductility, while the fine α_s phase restricts twin size and produces only slight deformation. Zhang et al[11] obtained an ultrafine α phase and the highest hardness in a TC21+3Mo alloy using the pseudo-spindle mechanism, because a finer α phase produces more α/β interfaces, which effectively hinder dislocation sliding and thereby increasing the hardness of the alloy. To some extents, the ductility of the alloy can be increased by increasing the α_p content. In addition, compared with spherical α_p phase, elongated α_p phase can reduce the interplanar spacing, resulting in a higher void density during deformation, and indicating that spherical α_p phases exert a more favorable effect on ductility than elongated α_p phases[12]. The α_p phase can provide a larger mean free path for dislocation motion, which is conducive to the activation of dislocation slip while inducing long-range stress concentration. Meanwhile, dislocations in the interconnected β_t regions can migrate between adjacent regions, which also helps to reduce stress concentration. During aging, the precipitation of the α_s phase

Received date: January 16, 2025
Foundation item: National Key Research and Development Program of China (2021YFB3700801)
Corresponding author: Liu Huiqun, Ph. D., Professor, School of Materials Science and Engineering, Central South University, Changsha 410083, P. R. China, E-mail: liuhuiqun@csu.edu.cn

increases the number of α/β interfaces and thus increases the resistance to dislocation motion, which contributes to strength improvement. The smaller the thickness of α_s and the higher the α_s content, the greater the number of α/β interfaces, leading to a more pronounced obstacle effect that impedes dislocation slip[13–15]. However, conventional heat treatment methods suffer from several drawbacks such as high heating temperatures and prolonged holding durations, leading to low efficiency, significant energy consumption, coarsening of primary grains, surface oxidation, and deterioration of mechanical properties. Furthermore, these methods often achieve strength enhancement at the expense of ductility.

Since Troitskii et al[16] first observed the electromigration effects in experiments where an electric current was applied to molten lead-tin and mercury-sodium alloys, pulsed current processing has emerged as an efficient technique. Driven by clean energy, it enables fast and precise current input, and has been widely employed to modulate the microstructure and enhance the mechanical properties of various metallic materials. In comparison to conventional heat treatment, pulsed current induces rapid alterations in the microstructure and properties of materials within milliseconds or even microseconds by influencing the dislocation motion, atomic diffusion, phase transformation, and recrystallization[17–18]. Yan et al[19] treated additively manufactured Ti-6Al-4V alloy using electrical pulses, and obtained a double-slab structure composed of α_p and α' phases. Compared with the conventional heat treatment, the application of pulsed current induced the formation of α' phases within the β matrix and inhibited the growth of α-slabs, resulting in a significant decrease in the average width of α-slabs, and thereby more effectively hindering dislocation slip. An electric pulse can promote atomic diffusion and defect reactions in TA15 alloy, so the electrostatic spheroidization of lamellar structure can be achieved. With the increase in current density and the prolongation of energization time, the spheroidization rate of the lamellar structure was increased, and the new interface strengthening of the spheroidized α phase ultimately resulted in a maximum hardness increase of 26.41% in material[20]. Zhu et al[21] found that in ZA27 alloys, the pulsed current accelerated dislocation motion and phase transformation, resulting in a 437% increase in elongation compared to samples without electric pulse treatment. The formability of the Ti-6Al-4V alloy was found to increase with the increase in both the frequency and peak current density of the electrical pulse. When the frequency was set to 250 Hz and the current density was set to 880 A/mm^2, a significant enhancement in formability by 52.2% was observed[22]. During the compression deformation of Ti-6Al-4V alloys, dynamic recrystallization and phase transformation were induced by electrical pulses, resulting in weakened texture strength. Compared to conventional forming techniques, this approach achieved an impressive formability increase of up to 417.9%[23]. Wang et al[24] realized the synergistic improvement of strength and elongation in Cu-14Sn-0.3Ti alloy by a combination of hot rolling and electric pulse treatment. Zhao et al[25] investigated the electroplastic deformation of Ti-Al (with 7at% Al) and observed that electrical pulses promoted cross-slip, resulting in the formation of a wavy dislocation morphology and enhanced twins, and thereby achieving a synergistic enhancement of both strength and ductility.

The high-density pulsed current (22.7 A/mm^2, 80 μs, 350 Hz, 5 min) induces rapid phase transformation in the Ti-6Al-4V alloy, and facilitates the preparation of a fine-grained microstructure with a grain size of 100 nm, which is smaller than that achieved through conventional heat treatment. This process leads to improved strength and elongation[26]. Xu et al[27] used high-density pulsed current to achieve an ultra-fast heating rate, raising the material temperature to 1000 ℃ within milliseconds. When treated by a subsequent aging process, the Ti-6A1-4V alloy exhibited high tensile strength (1358 MPa) and good elongation (14%). For aging-precipitation-type alloys, pulsed current can expedite the solute atom diffusion, resulting in more dispersed and evenly distributed precipitated phases within the matrix. Additionally, low-density pulsed current has been directly or indirectly integrated into the aging process of aluminum alloys, significantly reducing the aging time, conserving energy, and also enhancing the microstructure and properties of the material[28–32].

At present, research on the application of pulsed current in titanium alloys primarily focuses on high-density pulsed current. Dozens or even hundreds of amperes of currents induce a temperature rise of several hundred degrees Celsius in the sample within milliseconds, which leads to a thermal effect that cannot be ignored[33–34], and may even play a major role in performance improvement. To study the non-thermal effect of pulsed current, a low-density pulsed current that does not cause significant temperature rise is required. However, there are few studies on the application of low-density pulsed current in titanium alloys.

This work focuses on the application of low-density and short-duration pulsed current (1.8 A/mm^2, 60 s) in the heat treatment of titanium alloy. The effects of pulsed current-assisted aging on the microstructure and mechanical properties of the Ti-6Al-4V-0.5Mo-0.5Zr alloy were investigated, as well as the relationship between microstructure and mechanical properties through quasi-in-situ experiments. This research provides an industrially feasible heat treatment strategy for enhancing the strength and ductility of α+β dual-phase titanium alloys.

2 Experiment

2.1 Microstructure preparation

In this study, extruded Ti-6Al-4V-0.5Mo-0.5Zr alloy pipes were used with an outer diameter of 90 mm and a wall thickness of 9 mm. Table 1 presents the chemical composition of the alloy. The β-transus temperature (T_β) of the alloy was determined to be 965 ° C[13]. Fig. 1a illustrates the initial microstructure consisting of an elongated layered α_p and β_t phases along the rolling direction, with an alternating

Table 1 Chemical composition of Ti-6Al-4V-0.5Mo-0.5Zr alloy used in the experiment (wt%)

Al	V	Mo	Zr	Ti
6.33	3.69	0.63	0.79	Bal.

distribution of α_s and residual β phases within β_t.

To investigate the effect of pulsed current on microstructure, three solution temperatures and one aging temperature were selected, and a control group (without pulsed current) was set alongside the groups treated with pulsed current, resulting in six groups of samples (Fig. 1b). The solution treatments were performed at 890, 920, and 940 ℃ for 1 h, followed by air cooling (AC). All samples were then aged at 550 ℃ for 4 h. For the three pulsed current-assisted aging groups, after undergoing the same solution treatment as described above, the samples were placed in an aging furnace at 550 °C; pulsed current (parameters: frequency =500 Hz, duty cycle=50%, current density=1.8 A/mm^2, duration=60 s) was introduced, and aging was continued until the total 4 h of aging was reached after the current was turned off. The specific definition of the six groups of samples are shown in Table 2.

For pulsed current treatment, rod-like samples with a diameter of 6 mm and a length of 70 mm were cut along the extrusion direction of the Ti-6Al-4V-0.5Mo-0.5Zr alloy pipe by electrical discharge machining (Fig.2a–2b).

2.2 Mechanical tests

To test the tensile properties, the two ends of the samples were removed, and the remaining middle section was processed into rod-like tensile samples with a gauge diameter

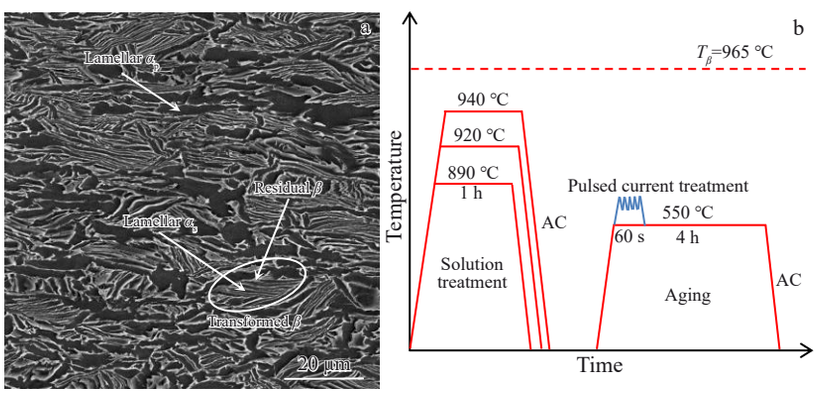

Fig.1 Initial microstructure of extruded Ti-6Al-4V-0.5Mo-0.5Zr alloy pipe (a) and schematic routes of heat treatment processes of six groups of samples (b)

Table 2 Heat treatment conditions of samples

Sample	Solution treatment	Aging treatment	Duration of pulsed current/s
S890A550	890 ℃/1 h/AC	550 ℃/4 h/AC	-
S920A550	920 ℃/1 h/AC	550 ℃/4 h/AC	-
S940A550	940 ℃/1 h/AC	550 ℃/4 h/AC	-
S890EA550	890 ℃/1 h/AC	550 ℃/4 h/AC	60
S920EA550	920 ℃/1 h/AC	550 ℃/4 h/AC	60
S940EA550	940 ℃/1 h/AC	550 ℃/4 h/AC	60
S920	920 ℃/1 h/AC	-	-
S920EA550-30s	920 ℃/1 h/AC	550 ℃/4 h/AC	30
S920A620A550	920 ℃/1 h/AC	620 ℃/60 s+550 ℃/4 h/AC	-

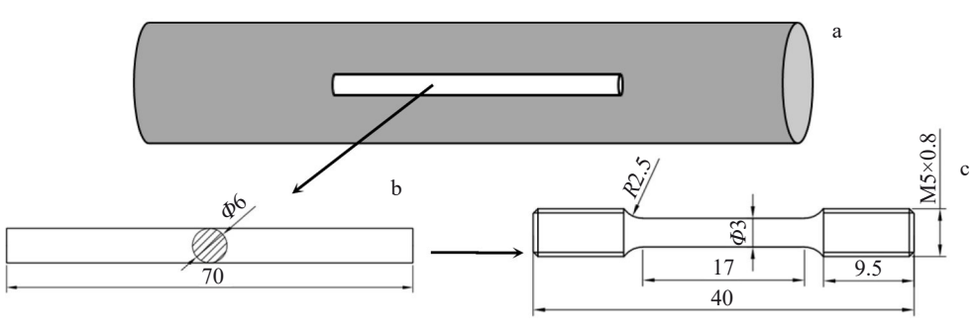

Fig.2 Schematic diagrams of rod-like sample cut from the alloy pipe (a), pulsed current-treated sample (b), and tensile sample (c)

of 3 mm, a gauge length of 15 mm, a parallel section length of 17 mm, and a total length of 40 mm, and the gripping end was threaded (Fig. 2c). Room-temperature tensile tests were performed using an MTS-858 testing machine with an initial stage rate of 0.8 mm/min followed by a two-stage rate of 2 mm/min. Three sets of parallel tensile samples were prepared to ensure the reliability of the test results.

2.3 Microstructure characterization

The microstructure of the Ti-6Al-4V-0.5Mo-0.5Zr alloy pipe was examined using scanning electron microscope (SEM, TESCAN CLARA), electron backscatter diffraction (EBSD, Oxford Symmetry S1), and transmission electron microscope (TEM, Tecnai G2F20 and Talos F200X). The samples for SEM observation were first mechanically polished and then etched with Kroll's reagent (10vol% HF+30vol% HNO_3+70vol% H_2O) for 15 s. For EBSD observation, the samples were mechanically polished on a specialized magnetic suction polishing disc for 40 min. The acquired EBSD data were analyzed using ATEX software[35]. TEM sample was initially thinned to 50 μm in thickness using sandpaper and then punched into wafers with 3 mm in diameter. Further thinning was performed through TenuPol-5 double-jet electrolysis using an electrolyte with the volume ratio of $HClO_4$: $CH_3(CH_2)_3OH$: CH_3OH=5:35:60. ImageJ software was employed to quantitatively measure the key microstructural parameters, including the volume fraction of α_p (V_{α_p}), volume fraction of β_t (V_{β_t}), diameter of α_p (D_{α_p}), and width of α_s (D_{α_s}).

2.4 Quasi-in-situ EBSD

To investigate the microstructure evolution of the alloy during pulsed current treatment, a quasi-in-situ EBSD analysis was conducted. The Ti-6Al-4V-0.5Mo-0.5Zr alloy sample was subjected to solution treatment at 920 °C for 1 h and subsequently air-cooled to room temperature (designated as S920). The surface was polished to meet the requirements for EBSD observation. Hardness measurements were performed at four points on the polished surface to define the observation region. EBSD analysis was performed on this region, and then the sample was treated with pulsed current at 550 °C for 30 s, followed by AC to room temperature (designated as S920EA550-30s). EBSD analysis was performed on the same region to track microstructural changes (Fig.3).

2.5 Temperature measurement during pulsed current treatment

To determine the temperature change of the sample induced by pulsed current, multiple measurements were conducted using thermocouples. Ultimately, upon application of short-duration pulsed current during aging at 550 °C, the temperature of sample rapidly increased from 550 °C to 620 °C; after the current disappeared, the temperature quickly decreased back to the set temperature of the aging furnace (Fig. 4). Consequently, it is concluded that the temperature rise caused by the low-density pulsed current employed in this study is approximately 70 °C, rendering its thermal effect on titanium alloy practically negligible.

3 Results

3.1 Microstructure evolution

According to SEM, EBSD, and TEM images, microstructure parameters, including V_{α_p}, V_{β_t}, D_{α_p}, and D_{α_s}, are shown in Table 3. Fig. 5 shows SEM microstructures of each sample, reflecting the microstructure characteristics of α_p and β_t phases across different experimental groups. Compared with the initial microstructure (Fig. 1a), significant variations are observed. The layered α_p phases, which are originally elongated along the extrusion direction, are transformed into an equiaxed structure. During solution treatment, the α-to-β phase transformation occurs, leading to a reduction in volume fraction of α_p and a significant increase in volume fraction of β_t. After solution at 890 °C followed by conventional aging, V_{α_p} and V_{β_t} are measured as 51.6% and 48.4%, respectively. As the solution temperature increases, V_{α_p} decreases, while V_{β_t} increases. For S920A550 sample, V_{α_p} decreases from 51.6% to 35.4%, while V_{β_t} increases from 48.4% to 64.6%. After solution treatment at 940 °C followed by aging, the V_{α_p} decreases by nearly 34% compared to the S890A550 sample. Furthermore, when the sample is cooled from the $\alpha+\beta$ dual-phase region after solution treatment, α_s phases precipitate from the β matrix; this precipitation process continues during the subsequent aging stage. The aging-induced α_s phases are

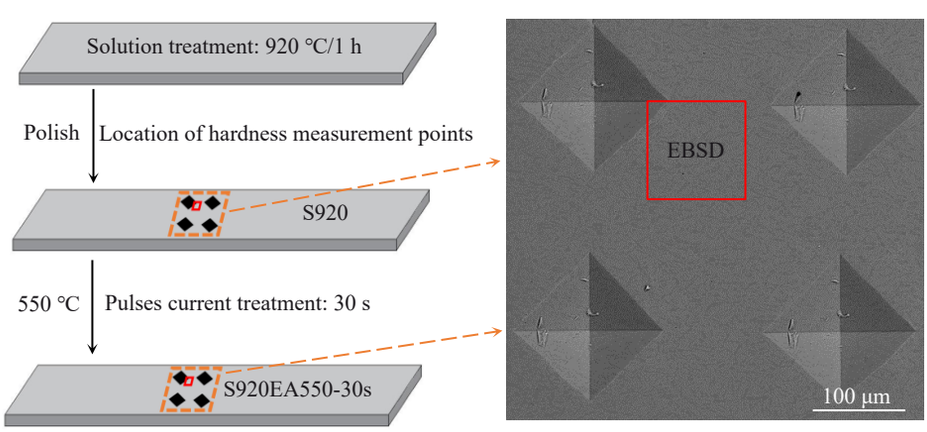

Fig.3 Schematic diagram of location for quasi-in-situ EBSD observation and hardness measurement

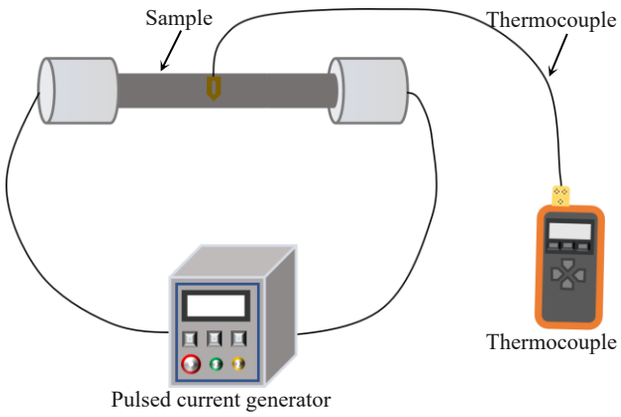

Fig.4 Temperature measurement during pulsed current treatment

Table 3 Microstructural parameters of V_{α_p}, V_{β_t}, D_{α_p}, and D_{α_s}

Sample	V_{α_p}/%	V_{β_t}/%	D_{α_p}/μm	D_{α_s}/nm
S890A550	51.6	48.4	3.92	75.8
S890EA550	54.9	45.1	4.64	48.5
S920A550	35.4	64.6	4.22	202.7
S920EA550	22.8	77.2	3.67	143.8
S940A550	10.7	89.3	5.92	194.6
S940EA550	7.6	92.4	3.47	147.8

confined between the preferentially precipitated lamellar layers formed during solution treatment. The thickness of these lamellar layers restricts the growth of α_s, ultimately resulting in finer aging-induced α_s phases. At relatively low solution treatment temperatures (e. g., 890 °C for sample S890A550), only a small quantity of fine α_s phases form with an average diameter of 75.8 nm. However, both the number and size of α_s phases increase as solution treatment temperatures rise. When the solution temperature approaches $\alpha \rightarrow \beta$ transformation temperature ($T_{\alpha/\beta}$) during solution treatment, the α_s phases are obviously coarsened to nearly 200 nm in size. A similar trend in microstructural changes can also be observed from S890EA550 to S940EA550; the microstructure analyses of α_s phases in these samples are conducted based on Fig.6 and Fig.7.

To compare the effects of pulsed current on V_{α_p}, V_{β_t}, and D_{α_s} during aging at the same solution temperature, the microstructure evolutions are observed at 890, 920, and 940 ℃. At 890 ℃, V_{α_p} increases slightly after pulsed current treatment. In contrast, an unexpected trend is observed at 920 and 940 ℃: under the action of pulsed current, V_{α_p} decreases while the corresponding V_{β_t} increases. For sample S920EA550, V_{α_p} decreases by 12.6% and V_{β_t} increases accordingly. For sample S940EA550, V_{α_p} decreases slightly from 10.7% (in the conventional aging counterpart S940A550) to 7.6%. It means that during the aging process, pulsed current may lead to the phase transformation from α_p to β phase, and subsequently β phase is transformed into β_t phase during the cooling process. In addition, it is worth noting that the pulsed current during aging also leads to the refinement of α_s. After solution treatment at 890 °C, the thickness of lamellar α in β_t structure is extremely fine, measuring only a few dozen nanometers, which is approximately one order of magnitude thinner than that of the α_s obtained after solution treatment at 920 or 940 ° C. The reduced α_s thickness facilitates rapid atomic diffusion, enabling easier phase transformation under pulsed current conditions. Consequently, during the initial cooling stage, β phase is more prone to transformation into α_p, connecting adjacent equiaxial α_p grains and ultimately forming a rod-like structure. This process leads to an increase in α_p content and a corresponding decrease in β_t content. After high-temperature solution treatment, pulsed current is more likely to facilitate the transformation from α to β phases. This results in a higher fraction of retained β phases during cooling, promoting the formation of β_t structure, which leads to a reduction in α_p content and an increase in β_t content. Therefore, the impact of pulsed current on the volume fraction of α_p is strongly dependent on the prior solution temperature.

Fig. 6 presents EBSD orientation maps of samples after solution and aging treatments. The black regions observed in all maps represent the unresolved nano-scale β phase. It is evident from Fig. 6a – 6c that the size of equiaxed α phase increases with the increase in solution temperature. This observation is consistent with the statistical results of D_{α_p} in Table 3, where D_{α_p} gradually increases from 3.92 μm to 5.92 μm. In addition, for samples solution-treated at 920 and 940 °C, D_{α_p} decreases significantly after pulsed current-assisted aging; however, it increases for the sample solution-treated at 890 °C with following pulsed current-assisted aging. Notably, the content of equiaxed α in the pulsed current-assisted aging samples is significantly lower than that in the conventional aging samples, while a certain amount of superfine lamellar structure emerges in the pulsed current-treated samples, which is consistent with the SEM results. In addition, these samples mainly have $< 2\bar{1}\bar{1}0 >$//rolling direction (RD) and $< 10\bar{1}0 >$// RD orientations. The orientation of grains does not change after the pulsed current is applied. A small number of < 0001 >// RD oriented grains are observed, and their fraction increases with increasing the solution temperature.

Fig. 7 presents TEM bright-field images of samples after solution and aging treatments. S920A550 and S920EA550 samples were discussed through selected area electron diffraction (SAED) analysis along the $[\bar{2}110]$ zone axis. The relationship between the α phase and the adjacent β phase obeys the classical Burgers relationship: $\{0001\}_\alpha // \{110\}_\beta$ and $< 11\bar{2}0 >_\alpha // <111>_\beta$ [36]. The orientation relationship between α and β in S890A550, S890EA550, S940A550, and S940EA550 samples also follows the above relationship[37–43].

It can be clearly seen that α_s phases are significantly refined in samples subjected to the same aging treatment after solution treatment at different temperatures. For samples solution-treated at 890 ° C, after conventional aging, fine needle-like α_s phases precipitate and interleave in different directions. After pulsed current-assisted aging, the volume fraction of α_s phase increases while their size decreases. For

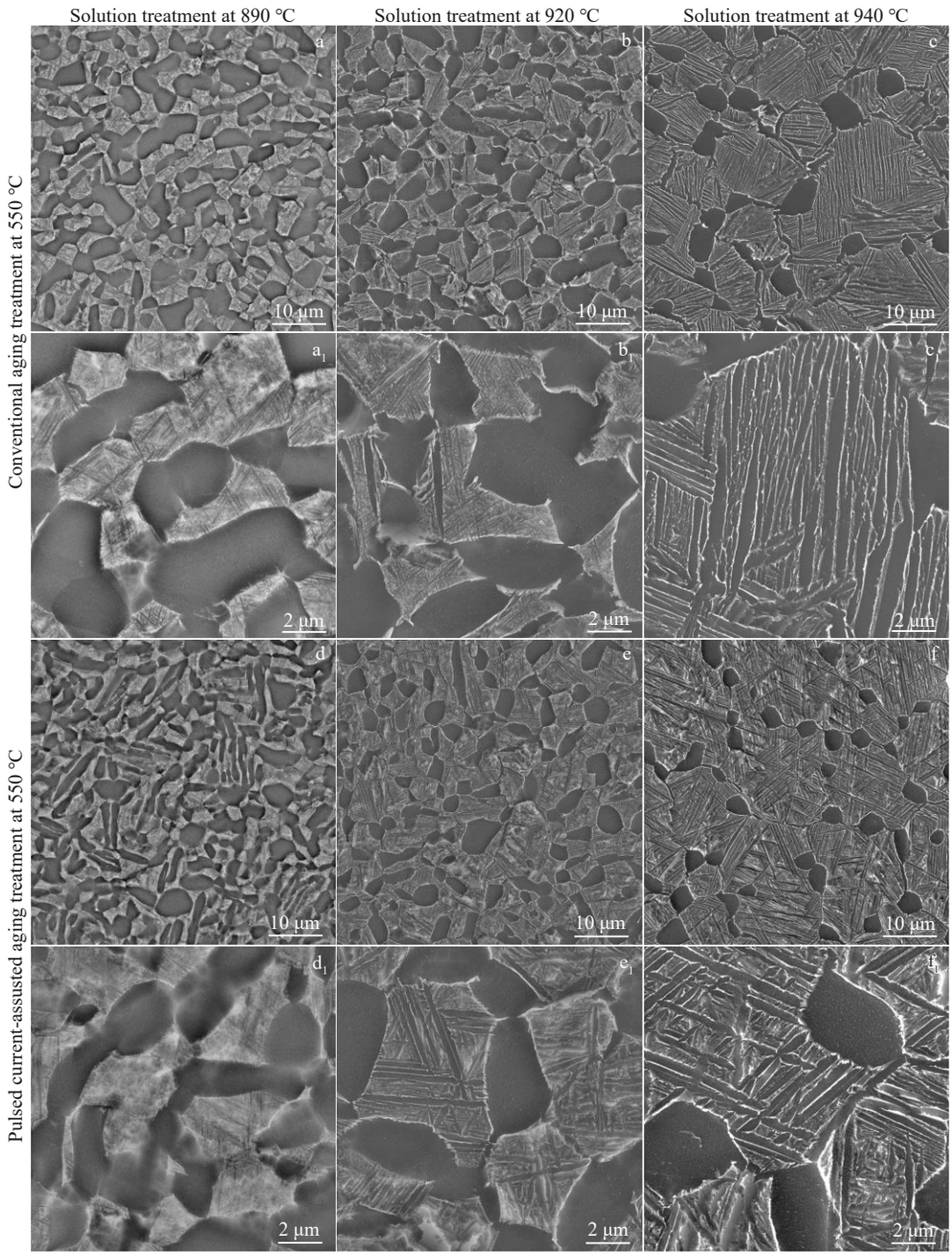

Fig.5 SEM images of solution-and-aging treated samples with and without pulsed current: (a, a_1) S890A550, (b, b_1) S920A550, (c, c_1) S940A550, (d, d_1) S890EA550, (e, e_1) S920EA550, and (f, f_1) S940EA550

the samples solution-treated at 920 and 940 °C (regardless of subsequent conventional aging or pulsed current-assisted aging), α_s phases are mainly distributed as parallel coarse lamellar structures. The difference is that for samples treated with pulsed current-assisted aging, the size of layered α_s between coarse lamellar structures is relatively small. The refinement effect is more obvious for the sample solution-treated at 920 °C followed by pulsed current-assisted aging.

In addition, α_s phases coarsen with increasing the solution temperature, particularly within the range from 890 ° C to 920 °C, resulting in a tenfold increase in the width of α_s. This phenomenon is attributed to the dependence of D_{α_s} on the thickness of residual β in β_t. After low-temperature solution and cooling treatments, the thickness of β_t structure in β_t regions is smaller, so α_s phases are finer after aging. Conversely, when the solution temperature exceeds 920 °C, a significant number of coarse α_s phases precipitate (Fig.$5b_1$–$5c_1$ and Fig. $5e_1$ – $5f_1$). During subsequent aging stage, fine α_s

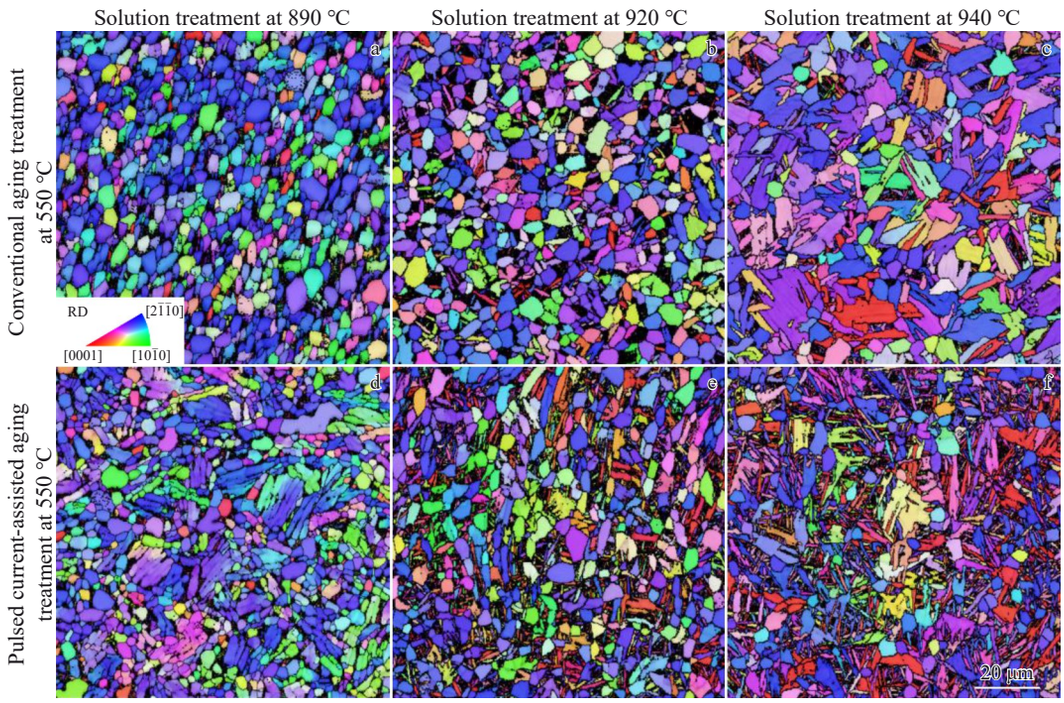

Fig.6 EBSD images of solution-and-aging-treated samples with and without pulsed current: (a) S890A550, (b) S920A550, (c) S940A550, (d) S890EA550, (e) S920EA550, and (f) S940EA550

phases precipitate between coarse lamellar structures, while further coarsening occurs for initially precipitated α_s phases[44].

3.2 Mechanical properties

The engineering stress-engineering strain curves of various samples are presented in Fig.8a. Table 4 provides the specific mechanical property data, including yield strength (YS), ultimate tensile strength (UTS), and elongation at break (EL). Overall, it can be observed that incorporating pulsed current during the aging process enhances the strength of alloy.

The S890EA550 sample exhibits high strength (YS=954 MPa and UTS=1063 MPa) and good ductility (EL=12.0%) in comparison to its conventional aging counterpart S890A550 (YS=948 MPa, UTS=1056 MPa, EL=12.6%). As the solution temperature increases to 920 °C, a significant decrease in strength is observed for S920A550 sample (YS=858 MPa and UTS=957 MPa), while EL remains as 12.1%. Notably, the S920EA550 sample presents a substantial increase in strength: YS increases by nearly 75 MPa and UTS increases by nearly 85 MPa, reaching 932 and 1042 MPa, respectively, without degrading ductility (EL=12.2%). Further increasing solution temperature to near the $T_{\alpha/\beta}$, the S940A550 sample exhibits slightly higher strength and a slightly decreased ductility compared to S920A550: YS=874 MPa, UTS=997 MPa, EL=11.4%. For S940EA550, pulsed current results in an increase in strength (YS=906 MPa and UTS=1022 MPa) and an EL level (EL=11.3 %) similar to that of S940A550.

Therefore, among samples subjected to conventional heat treatment (without pulsed current) at different solution temperatures, the S890A550 sample exhibits excellent strength and ductility. However, pulsed current does not consistently exert a significant strengthening effect during the aging process. For samples S920EA550 and S940EA550, the strengthening effect of pulsed current is highly significant, whereas its effect on the S890EA550 sample is minimal. In general, the grain size of α phase (α_p and α_s) and the distribution of intergranular β phases determine the strength, while the ductility is influenced by multiple factors, such as grain orientation, α colony size, the thickness of lamellar α_s, and the distribution characteristics of α_p. During plastic deformation, the β phase, which demonstrates a non-Schmidt effect, can significantly accommodate the plastic deformation of the surrounding α phases, which have limited slip systems. Specifically, within the β_t regions, intergranular β phases facilitate the transfer of dislocations between adjacent α grains (slip transfer events), thereby markedly reducing stress concentrations caused by slip blockages between α colonies with differing orientations. Additionally, during the stage of inhomogeneous plastic deformation, intergranular β phases can deflect transgranular cracks initiated in α_s phases, which is also advantageous for enhancing toughness. Consequently, β_t content may have a positive influence on ductility. However, a high β_t content does not necessarily leads to higher plastic deformation capability. This capacity is also contingent upon the size of β_t regions, as well as the size and morphology of α colonies within β_t. Compared with that of its conventional aging sample S890A550, the β_t content of sample S890A550 (after 890 °C solution treatment and pulsed current aging) is slightly reduced, resulting in a slight decrease in EL. Although the thickness of the aging-induced α_s decreases and its content increases, which should enhance strengthening effect, the

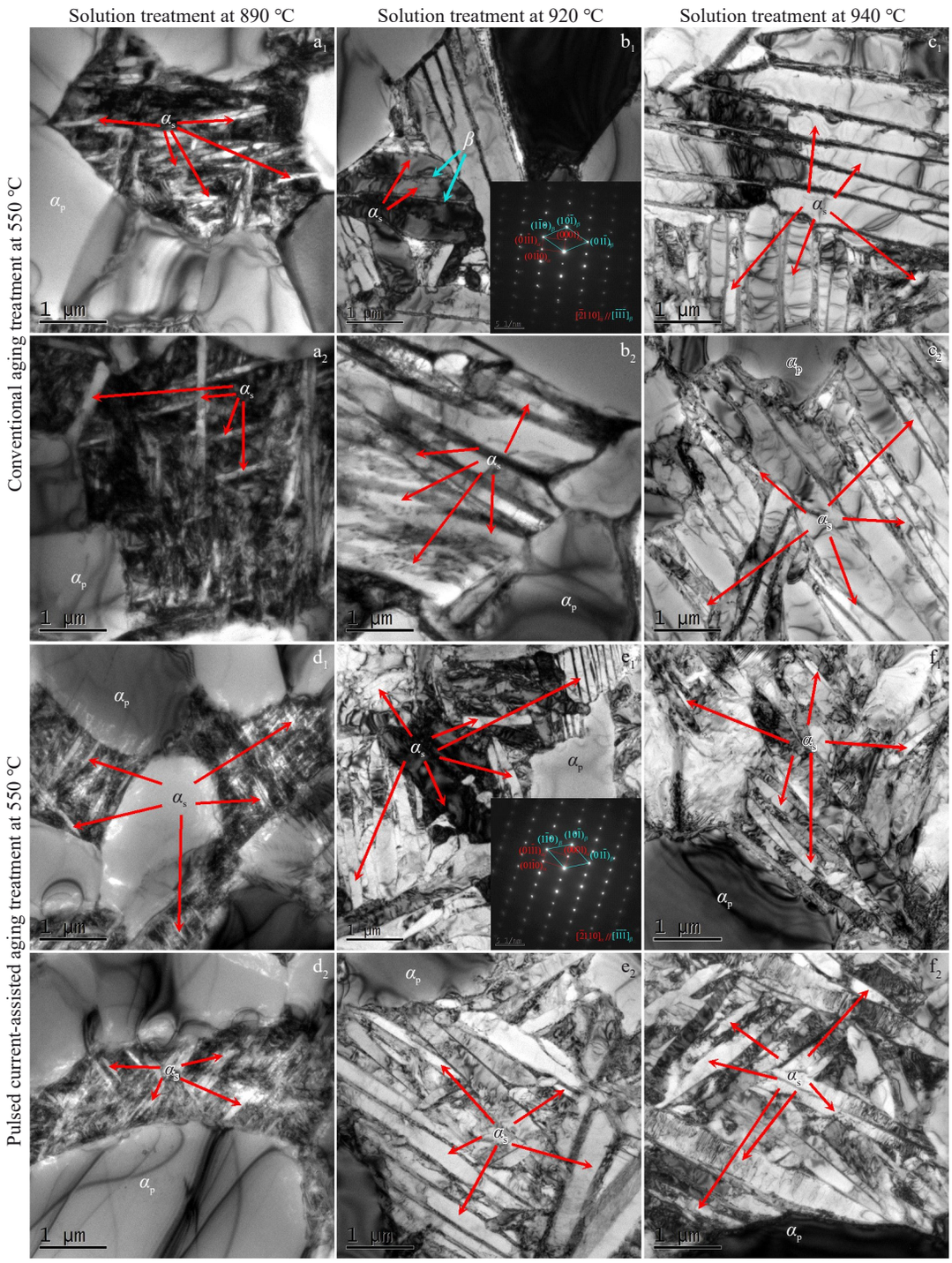

Fig.7 TEM images of different samples: (a_1, a_2) S890A550, (b_1, b_2) S920A550, (c_1, c_2) S940A550, (d_1, d_2) S890EA550, (e_1, e_2) S920EA550, and (f_1, f_2) S940EA550

increase in α_p size weakens the strengthening effect, so the final strength only increases slightly. The strengthening effect of pulsed current on S890EA550 is far less pronounced than that on samples solution-treated at 920 and 940 °C. This means that the microstructure obtained after different solution treatments is a pivotal factor influencing the subsequent pulsed current-assisted aging.

Based on the above measurement results of temperature rise of the alloy under pulsed current, a corresponding conventional heat treatment was performed as follows: the alloy was first solution-treated at 920 °C for 1 h and air-cooled to room temperature; it was then heat-treated at 620 °C for 1 min (matching the duration of pulsed current application in the experimental group) before being immediately aged at 550 °C for 4 h followed by AC. This control sample was designated as S920A620A550. The tensile curves of samples S920A550, S920A620A550, and S920EA550 are shown in Fig. 8b. It is evident that the sample S920EA550 subjected to pulsed

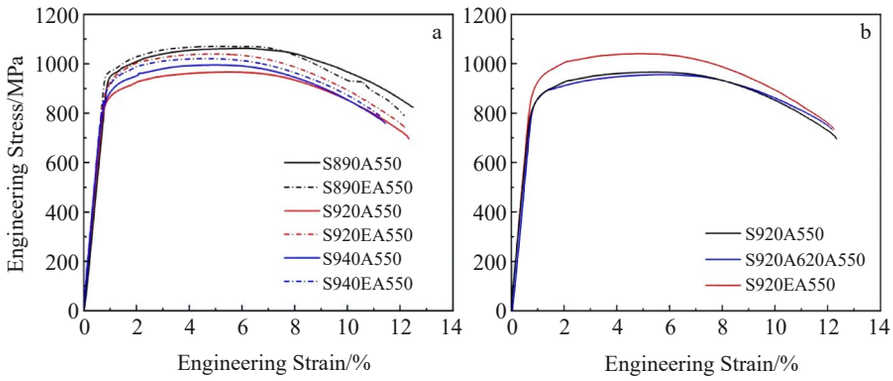

Fig.8 Engineering stress-engineering strain curves of samples solution-treated at 890, 920, and 940 °C followed by conventional aging or pulsed current-assisted aging (a); engineering stress-engineering strain curves of samples solution-treated at 920 °C under conventional aging, pulsed current-assisted aging, and stepwise aging (b)

Table 4 Tensile properties of solution-and-aging treated samples with and without pulsed current treatment

Sample	YS/MPa	UTS/MPa	EL/%
S890A550	948±17	1056±7	12.6±0.1
S890EA550	954±18	1063±10	12.0±0.1
S920A550	858±3	957±9	12.1±0.1
S920EA550	932±1	1042±3	12.2±0.4
S940A550	874±9	997±5	11.4±0.1
S940EA550	906±16	1022±15	11.3±0.4

current-assisted aging exhibits the highest strength. Moreover, the tensile curves of sample S920A550 (conventional aging) and sample S920A620A550 (stepwise aging with the first-step temperature matching the pulsed current-induced temperature rise) almost completely overlap. This indicates that the thermal effect of low-density pulsed current used in this study is not responsible for strength increase. Instead, the strengthening effect of pulsed current-assisted aging is mainly attributed to the electrical effect of the pulsed current.

The fracture morphologies of all samples are illustrated in Fig.9, revealing a ductile fracture mode. The fracture surfaces consist of a central fibrous area and an external shear lip region with numerous dimples. It is evident that the dimples on the fracture surfaces of samples S890A550, S890EA550, S920A550, and S920EA550 are relatively deep and large, which corresponds to the slightly higher EL values reported in Table 4. However, from the fracture morphology, it seems that

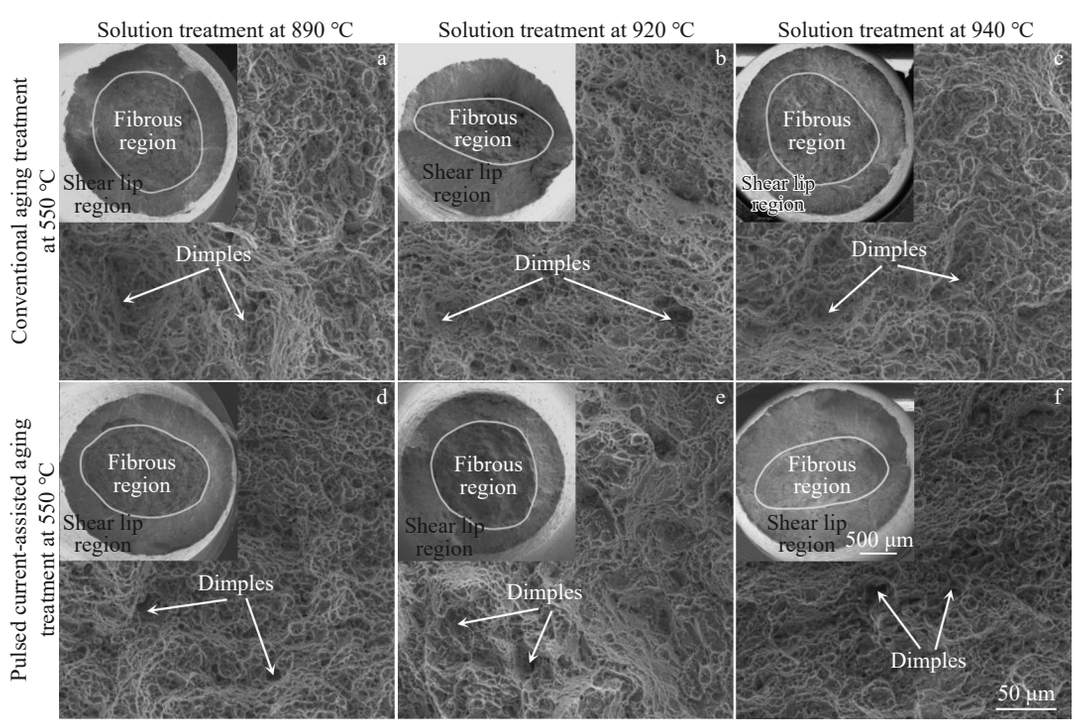

Fig.9 Fracture morphologies of different samples: (a) S890A550, (b) S920A550, (c) S940A550, (d) S890EA550, (e) S920EA550, and (f) S940EA550

the source of the strength difference caused by the pulsed current cannot be found. So, further microstructural analysis and discussion are needed.

4 Discussion

4.1 Quasi-in-situ EBSD analysis of microstructure evolution during pulsed current treatment

Fig. 10 illustrates the results of quasi-in-situ EBSD observation. Overall, there is a significant difference between the microstructures before and after pulsed current treatment. This is particularly evident in the white dashed line regions, where uniform refinement of α_p (Fig. 10a_1 – 10b_1) and precipitation of fine lamellar α_s at grain boundaries can be clearly seen. When pulsed current flows through the metal, the localized Joule heating effect may rapidly induce phase transformations at a relatively low temperature by generating instantaneous high temperatures at crystal defects. Additionally, strong scattering of drifting electrons can provide extra energy to lower the activation energy for atomic diffusion and facilitate the α-to-β phase transformation[45]. Consequently, pulsed current effectively promotes the phase transformation by reducing the transformation temperature and shortening the transformation duration[46–47]. It can be observed that the dissolution of some α phases and precipitation of fine α phases mainly occur at the grain boundary. Because phase boundaries and grain boundaries serve as preferential channels for electron migration over the grain interior, electron migration leads to localized temperature elevation in these areas, which may promote the phase transformation. Notably, while the transition of α_p to β_t is a common phenomenon, as shown by the white dashed arrows in region D of Fig. 10, occasional instances are observed: α_p-to-α_p transition with different orientations and β_t-to-α_p transition, as denoted by the white and yellow arrows in regions A, B, and C in Fig. 10. The dissolution of α phases and subsequent transformation from β phases back to α phases occur randomly. Specifically, the dissolution of α phase can take place within either α_p or lamellar α_s phases within β_t regions. Furthermore, the transformed β phase can be transformed into either α_p or β_t phases.

Fig. 11 and Table 5 further display the orientation relationships between the pre-transformation α phase (pre-α) and post-transformation α phase (post-α) for the above phase transitions. For pre-α_p to post-α_p transition, the two α phases generally maintain an orientation relationship of $<10\bar{1}0>_{pre\text{-}\alpha}$// $<10\bar{1}0>_{post\text{-}\alpha}$. Not all such transitions follow this orientation relationship. Interestingly, if a pre-α_p grain is not fully dissolved during the transition, the post-α_p grain retains the $<10\bar{1}0>_{pre\text{-}\alpha}$ //$<10\bar{1}0>_{post\text{-}\alpha}$ orientation. In contrast, if the pre-α_p grain is dissolved completely, the post-α_p grain exhibits no orientation relationship with the pre-α_p. As for transition of pre-β_t to post-α_p (Fig. 11b), the post-α_p grain also shows no $<10\bar{1}0>_{pre\text{-}\alpha}$ // $<10\bar{1}0>_{post\text{-}\alpha}$ orientation with any α_s in β_t, even though pre-β_t region is partially dissolved. In the case of pre-α_p to post-β_t transition, the pre-α_p is segmented into multiple regions, in which V2 and V4 grains seem to be undissolved portions of the pre-α_p, while V1 and V3 grains are newly formed α_p grains that exhibit no orientation relationship with the pre-α_p. Indeed, a substantial transition of pre-α_p to post-α_p does not follow the above orientation relationship; instead, these transitions result in post-α_p with random orien-

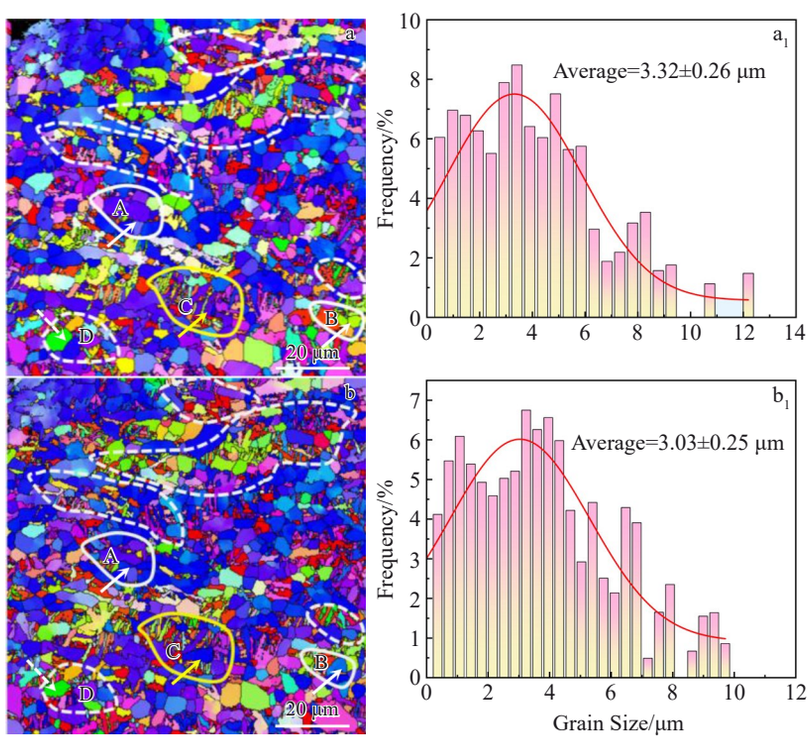

Fig. 10 Quasi-in-situ microstructures (a–b) and grain size statistics (a_1–b_1) of different samples: (a, a_1) S920A550 and (b, b_1) S920EA550-30s

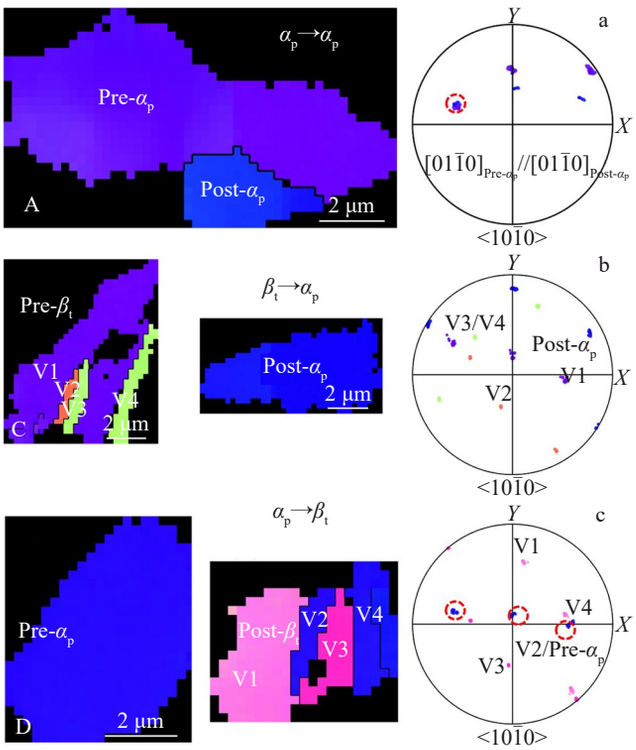

Fig.11 Three types of phase transition induced by pulsed current in regions A, C, and D marked in Fig. 10: (a) pre-α_p to post-α_p, (b) pre-β_t to post-α_p, and (c) pre-α_p to post-β_t

tations. This can be attributed to the β-to-α phase transformation involving multiple variant selections.

Combining the quasi-in-situ EBSD results with SEM images and the statistical data in Table 3, which collectively indicate that pulsed current-assisted aging reduces α_p content and increases β_t content, it is reasonable to speculate that the pulsed current intensely promotes the α_p-to-β phase transition even at low temperatures. After the pulsed current disappears, the newly formed β phases are predominantly transformed into β_t phases. Similarly, Xiao et al[48] demonstrated that pulsed current application to a Ti-6Al-4V alloy promoted α-to-β phase transition, leading to a rapid increase in ductility. Applying pulsed current at relatively low temperatures and short durations facilitated grain refinement and increased proportion of β_t, indicating its role in initiating the α-to-β phase transition process[29]. Compared to traditional heat treatment methods, pulsed current requires less energy to drive the α-to-β phase transition in Ti-6Al-4V alloy[30].

4.2 Strengthening mechanism

The microstructural evolution exerts a decisive influence on the material properties of the alloy. Zhu et al[47] proposed that the strength of titanium alloys is intricately associated with the size and morphology of α_s phases, while ductility is primarily governed by the compatible deformation between α_p phases and β matrix. The precipitation of α_s within the β_t results in a large number of α_s/β phase boundaries. Furthermore, during tensile deformation, the orientation deviation between α_s colonies in an α/β cluster obviously influences the dislocation slip. The smaller the orientation deviation, the greater the likelihood of a slip transfer event. The α/β cluster, which is composed of α_s colonies with multiple orientations, significantly enhances the slip blockage events. Consequently, the volume fraction of such α/β cluster directly affects the strength.

This work evaluates the influence of pulsed current on the grain orientations within α_p and β_t regions by directly calculating the angles between the basal planes and the loading axis in the quasi-in-situ EBSD area, and the results are shown in Fig. 12. It can be found that after pulsed current-assisted aging for 30 s, the fraction of α grains with basal plane-loading axis angles fluctuated in the range of 0° – 20° increases, while the fraction of grains with angles fluctuated in the range of 55° – 75° decreases, which intensifies the difference in fraction between low-angle and high-angle orientations. The main change caused by the pulsed current-assisted aging is the formation of β_t regions, so it can be inferred that the pulsed current promotes an increase in β_t content and simultaneously facilitates the formation of α colonies with multiple types within the newly formed β_t, which can provide a positive effect on strength.

The presence of grain boundary pinning and numerous fine lamellar α_s enhances alloy strength; however, it also leads to

Table 5 Misorientation and axes between pre-α phase and post-α phase in Fig.11

Event	Region	Misorientation/(°)	Axis
Pre-α_p→post-α_p	-	23.0342	[−0.1081, −0.7980, 0.9060, −0.2281]
Pre-β_t→post-α_p	V1/post-α_p	64.3095	[0.6650, −0.9599, 0.2949, −0.2894]
	V2/post-α_p	69.4836	[−0.9501, 0.5314, 0.4187, −0.4873]
	V3/post-α_p	35.8760	[−0.8763, 0.3841, 0.4922, 0.7624]
	V4/post-α_p	36.4873	[−0.8805, 0.3905, 0.4899, 0.7511]
Pre-α_p→post-β_t	Pre-α_p/V1	59.7917	[−0.0953, 0.9015, −0.8061, 0.2199]
	Pre-α_p/V2	0.5826	[0.8874, −0.8367, −0.0507, 0.1291]
	Pre-α_p/V3	64.0450	[0.8203, 0.0128, −0.8331, −0.4750]
	Pre-α_p/V4	2.5312	[0.4130, −0.9526, 0.5395, 0.4717]

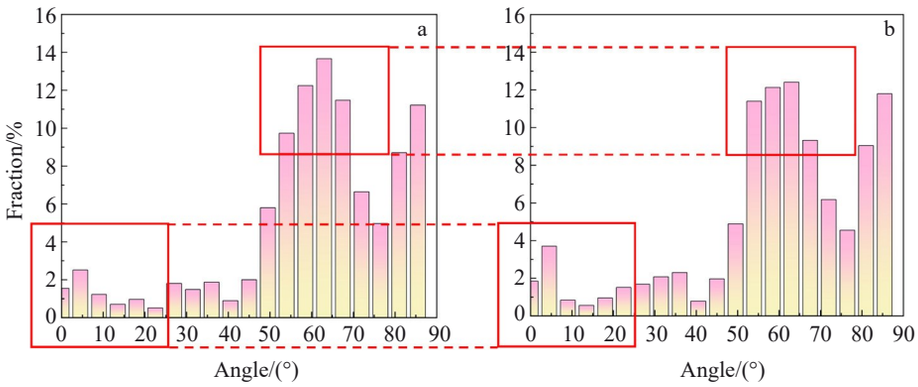

Fig.12 Fractions of basal plane-loading axis angles of samples before (a) and after (b) pulsed current-assisted aging

uneven local strain distribution and reduced ductility. In this study, due to the low solution temperature of the S890A550 sample, V_{α_p} in the microstructure is nearly 50%, D_{α_p} is 3.92 μm, and the D_{α_s} is only 75.8 nm. These microstructural features increase the number of α_p/β and α_s/β phase boundaries, which hinders the dislocation slip during plastic deformation, thereby enhancing grain refinement strengthening. Meanwhile, the interconnected β_t reduces long-range stress concentration, resulting in superior strength and ductility. Unsurprisingly, increasing the solution temperature leads to a decrease in V_{α_p} and a slight increase in D_{α_p}, consequently diminishing the strengthening effect, as observed in S920A550 and S940A550 samples. In contrast, for S920EA550 and S940EA550 samples, the grain refinement caused by pulsed current leads to an increase in the number of grain boundaries, resulting in a remarkable strengthening effect. Compared to single-phase microstructures, composite multiphase microstructures exhibit work hardening behavior. The disparity in deformability between soft and hard phases results in strain incompatibility at both the phase interface and grain boundary, consequently leading to dislocation accumulation. The contrasting mechanical properties of β_t/α_p and β/α_s within titanium alloys facilitate the accumulation of geometrically-necessary dislocations (GNDs). Subsequently, These GNDs hinder dislocation slip and contribute to work hardening and strength enhancement of the multiphase titanium alloys[49–50]. The alloy subjected to solution treatment in the $\alpha+\beta$ dual-phase region exhibits better ductility than that in the β single-phase region. This is attributed to two key factors. Firstly, the soft α_p phase has sufficient plastic deformation capacity to coordinate the deformation between lamellar structures, while the hard β_t structure (filled with lamellar α_s phase) severely restricts the sliding space of dislocations. Secondly, the β grain size of the solution-treated alloy in the $\alpha+\beta$ region is smaller than that in β region. The α_p phase at the β grain boundary can effectively inhibit the growth of the β grain, and small-sized grains facilitate synergistic deformation between grains, thus improving the ductility of the alloy[51–53]. For heterogeneous materials, uneven strain distribution during deformation leads to the accumulation of GNDs at interfaces, forming a strain gradient. This gradient generates back stresses and forward stresses on soft and hard phases, respectively, enabling the synergistic improvement of strength and ductility[54]. Similarly, in this work, the multi-oriented α_s colonies and interconnected β_t structures can also promote the accumulation of GNDs, which may lead to a potential heterogeneous deformation induction (HDI) effect.

5 Conclusions

1) In Ti-6Al-4V-0.5Mo-0.5Zr alloy, a large number of α_p phases dissolve during pulsed current-assisted aging, and the resulting β phases are then randomly transformed into either new equiaxed α phases or β_t phases. This process can greatly refine both the α_p grains and the grains in β_t regions.

2) During the pulsed current-assisted aging process, α_p-to-β_t transition is the dominant reaction, while the α_p-to-α_p transition is less common. The α_s colonies in β_t regions formed by α_p transformation have multiple orientation types, i. e., there are multiple variant selections. For the α_p-to-α_p transition: if the pre-α_p grains are not fully dissolved, the post-α_p grains maintain the $<10\bar{1}0>$pre-α_p // $<10\bar{1}0>$post-α_p orientation relationship; if the pre-α_p grains are completely dissolved, the newly formed post-α_p grains no longer follow this orientation relationship.

3) Pulsed current-assisted aging significantly improves the strength of alloy while preserving its ductility. The improvement of strength is mainly due to the formation of a large number of β_t phases and the refinement of α_p grains. In addition, the multi-oriented α_s colonies increase the slip resistance of dislocations in β_t region and enhance the strengthening effect of β_t, which may induce a potential HDI effect, resulting in excellent strain hardening ability and ductility.

References

1 Antunes R A, Salvador C A F, Oliveira M C L. *Materials Research*[J], 2018, 21: e20170979

2 Mosallanejad M H, Abdi A, Karpasand F *et al*. *Advanced Engineering Materials*[J], 2023, 25(24): 2301122

3 Ahmed H A, Modar S, Hayam A A *et al*. *Metals and Materials*

International[J], 2024, 30: 1

4 Chiu W, Hayakawa R, Nohira N *et al*. *Journal of Alloys and Compounds*[J], 2024, 991: 174509

5 Li Z, Wo J, Fu Y Y *et al*. *ACS Biomaterials Science & Engineering*[J], 2023, 9(12): 6935

6 Wang Z W, Cheng H C, Liu B *et al*. *Metals*[J], 2022, 12(6): 1025

7 Liu Y K, Peng S X, Wang B *et al*. *Fatigue & Fracture of Engineering Materials & Structures*[J], 2024, 47(6): 1883

8 Peng S X, Liu Y K, Fu M Z *et al*. *Materials Science and Engineering A*[J], 2024, 895: 146217

9 Wang L, Zhao X H, Wang X D *et al*. *Coatings*[J], 2024, 14(8): 941

10 Jing R, Liang S X, Liu C Y *et al*. *Materials Science and Engineering A*[J], 2012, 552: 295

11 Zhang L, Tang J L, Wang Z Y *et al*. *Rare Metals*[J], 2021, 40(8): 2099

12 Wang Z Y, Liu L B, Zhang L G *et al*. *Materials Transactions*[J], 2019, 60(2): 269

13 Chi G F, Yi D Q, Jiang B *et al*. *Journal of Alloys and Compounds*[J], 2021, 852: 156581

14 Xu J W, Zeng W D, Zhao Y W *et al*. *Materials Science and Engineering A*[J], 2016, 676: 434

15 Lao Z H, Zhang H Y, Wang S Y *et al*. *Rare Metal Materials and Engineering*[J], 2024, 53(9): 2430

16 Troitskii O A. *Materials Science and Engineering*[J], 1985, 75(1–2): 37

17 Su J L, Jiang F L, Teng J *et al*. *Rare Metals*[J], 2024, 43(12): 6288

18 Wang Xiaotong, Zhao Tong, Wang Yuan *et al*. *Rare Metal Materials and Engineering*[J], 2023, 52(5): 1683 (in Chinese)

19 Yan X D, Xu X F, Zhou Y C *et al*. *Journal of Materials Science & Technology*[J], 2024, 193: 37

20 Yan Siliang, Shi Yingbin, Zhang Xiaoli *et al*. *Rare Metal Materials and Engineering*[J], 2023, 52(5): 1783 (in Chinese)

21 Zhu Y H, Jiang Y B, Liu X M. *Journal of Alloys and Compounds*[J], 2018, 737: 630

22 Ao D W, Chu X R, Gao J *et al*. *The International Journal of Advanced Manufacturing Technology*[J], 2019, 104: 4243

23 Ao D W, Gao J, Chu X R *et al*. *International Journal of Solids and Structures*[J], 2020, 202: 357

24 Wang Yuxuan, Zou Juntao, Feng Qiaoli *et al*. *Rare Metal Materials and Engineering*[J], 2024, 53(4): 1155 (in Chinese)

25 Zhao S T, Zhang R P, Chong Y *et al*. *Nature Materials*[J], 2020, 20(4): 468

26 Zhao Z Y, Wang G F, Zhang Y L *et al*. *Journal of Alloys and Compounds*[J], 2019, 786: 733

27 Xu X F, Yan X D, Qian Y *et al*. *Journal of Alloys and Compounds*[J], 2021, 899: 163303

28 Chen K, Zhan L H, Xu Y Q *et al*. *Journal of Materials Research and Technology*[J], 2020, 9(6): 15433

29 Kang K J, Li D Y, Gao G L *et al*. *Metals*[J], 2019, 9(10): 1103

30 Liu Y Z, Huang M H, Ma Z Y *et al*. *Journal of Alloys and Compounds*[J], 2016, 673: 358

31 Xu Y Q, Tong C Y, Zhan L H *et al*. *The International Journal of Advanced Manufacturing Technology*[J], 2018, 97: 3371

32 Yu S R, Xu K R, Wang T *et al*. *Materials Science and Engineering A*[J], 2024, 909: 146814

33 Arka L, Pratheek S, Franz R. *Modelling and Simulation in Materials Science and Engineering*[J], 2019, 27(8): 085006

34 Kim M J, Yoon S, Park S *et al*. *Applied Materials Today*[J], 2020, 21: 100874

35 Beausir B, Fundenberger J J. *Analysis Tools for Electron and X-ray Diffraction, ATEX Software*[EB/OL]. www.atex-software.eu

36 Fu X Q, Wang X D, Zhao B K *et al*. *Nature Materials*[J], 2022, 21(3): 290

37 Bhattacharyya D, Viswanathan G B, Denkenberger R *et al*. *Acta Materialia*[J], 2003, 51(16): 4679

38 Bhattacharyya D, Viswanathan G B, Fraser H L. *Acta Materialia*[J], 2007, 55(20): 6765

39 Germain L, Gey N, Humbert M *et al*. *Acta Materialia*[J], 2008, 56(16): 4298

40 Qiu D, Shi R, Zhang D *et al*. *Acta Materialia*[J], 2015, 88: 218

41 Seward G G E, Celotto S, Prior D J *et al*. *Acta Materialia*[J], 2004, 52(4): 821

42 Shi R, Dixit V, Fraser H L *et al*. *Acta Materialia*[J], 2014, 75(15): 156

43 Stanford N, Bate P S. *Acta Materialia*[J], 2004, 52(17): 5215

44 Ma Xin, Sun Qianjiang, Wen Chao *et al*. *Rare Metal Materials and Engineering*[J], 2023, 52(12): 4260 (in Chinese)

45 Bao J X, Chen W J, Bai J N *et al*. *Materials Science and Engineering A*[J], 2021, 831: 142262

46 Zhao Y X, Peng L F, Lai X M. *Journal of Materials Processing Technology*[J], 2018, 261: 12

47 Zhu R F, Liu J N, Tang G Y *et al*. *Journal of Alloys and Compounds*[J], 2014, 584: 225

48 Xiao A, Yan Z Q, Huang C Q *et al*. *Materials Science and Engineering A*[J], 2023, 877: 145188

49 Ashby M F. *The Philosophical Magazine: A Journal of Theoretical Experimental and Applied Physics*[J], 1970, 21(170): 399

50 De F C, Brulard A, Vivès S *et al*. *Materials Research Letters*[J], 2016, 5(3): 201

51 Zhang L G, Zhou J Y, Wang Z Y *et al*. *Materials Research Express*[J], 2020, 7(2): 026541

52 Shekhar S S, Sarkar R, Kar S K *et al*. *Materials & Design*[J], 2015, 66: 596

53 Wang X, Lv F, Shen L D *et al*. *Acta Metallurgica Sinica* (*English Letters*)[J], 2019, 32(9): 1173

54 Wu D, Hao M Y, Zhang T L *et al*. *Acta Materialia*[J], 2023, 257: 119182

无延展性损失下低密度脉冲电流诱导细化次生α相强化 Ti-6Al-4V-0.5Mo-0.5Zr合金

涂燕妮[1]，罗　威[1]，刘会群[1,2]，凤伟中[3]，张平辉[3]

(1. 中南大学 材料科学与工程学院，湖南 长沙 410083)

(2. 中南大学 粉末冶金国家重点实验室，湖南 长沙 410083)

(3. 宝鸡钛业股份有限公司，陕西 宝鸡 721014)

摘　要：对不同固溶处理的Ti-6Al-4V-0.5Mo-0.5Zr合金进行了低密度短时脉冲电流辅助时效处理。结果表明，脉冲电流辅助时效过程中，大量的α_p相回熔转变为新的β相，然后新β相主要转变为β_t组织或偶尔转变为新的α_p相，导致晶粒显著细化，尤其是层片状α_s相。与常规时效相比，脉冲电流辅助时效过程在保持相同延展性的同时显著提高了强度，实现了屈服强度932 MPa、抗拉伸强度1042 MPa和延伸率12.2%的优异组合。这主要归因于β_t组织含量的增加、明显的晶粒细化效应以及β_t区域内多个变体α_s集束的滑移阻碍作用。

关键词：钛合金；脉冲电流；组织细化；强度；延展性

作者简介：涂燕妮，女，1999年生，硕士，中南大学材料科学与工程学院，湖南 长沙 410083，E-mail：223112093@csu.edu.cn